Combustion and Flame 245 (2022) 112364

Contents lists available at ScienceDirect

Combustion and Flame

journal homepage: www.elsevier.com/locate/combustflame

Triple flames in swirling flows

Xiao Zhang[a,b,*], Joseph D. Chung[c], Elaine S. Oran[a]

[a] Dept. of Aerospace Engineering, Texas A&M University, College Station, TX, 77843
[b] Dept. of Aerospace Engineering, University of Maryland, College Park, MD, 20742
[c] Independent Scholar

ARTICLE INFO

Article history:
Received 20 January 2022
Revised 28 August 2022
Accepted 29 August 2022

Keywords:
Triple flame
Vortex flow
Vortex breakdown
Blue whirl

ABSTRACT

Recent work has shown that the blue whirl, a soot-free hydrocarbon flame, is comprised of a triple flame in a swirling flow undergoing vortex breakdown. This paper describes three-dimensional, numerical simulations of triple flames in swirling flows with and without vortex breakdown and relates this to what is known about the blue whirl. The results for three swirl numbers are presented, all of which develop a triple flame. The shape of the triple flame, however, differs depending on whether there is vortex breakdown and its location. Changes in vorticity before and after ignition are examined for each case. The analysis shows that for the lowest swirl number, the effect of volume expansion dominates and mitigates vortex breakdown. Increasing swirl results in vortex stretching and tilting becoming dominant and promoting vortex breakdown. Which of these effects is dominant determines the flow structure and then the flow structure determines the different flame shapes. Insights gained from this work and their relation to the blue whirl are discussed.

1. Introduction

The blue whirl [1] (Fig. 1c) is a stable, quiet, spinning blue flame that evolves naturally in experiments from a partially confined yellow fire whirl. The blue whirl has been shown to burn many different liquid hydrocarbon fuels (e.g., whiskey, heptane, crude oil) with no soot formation [1–3]. It also burns fuels contaminated by water. The high combustion efficiency makes the blue whirl a potential source for clean power production with fuel flexibility. Recently, the flame and flow structure of the blue whirl was theoretically and numerically analyzed in [4,5]. As shown in Fig. 1, the blue whirl is composed of a diffusion flame, which is the purple crown, a premixed lean flame surrounding the purple crown on the outside, and a premixed rich flame on the bottom under the ring. These three flames meet at the blue ring to form a triple flame. Numerical simulations [4,5] also showed that the blue whirl emerges as a result of vortex breakdown in swirling flows. As shown in Fig. 1b, there is a recirculation region, which is a bubble mode of vortex breakdown inside the blue whirl. The blue whirl is a unique combination of flame and flow structure – a triple flame in a swirling flow with vortex breakdown, and there have been few studies of this structure to date. Fundamental understanding of triple flames in swirling flows, on one hand, is necessary to control the blue whirl and create it at will as a clean energy source. On the other hand, such studies also provide additional understanding of combustion in swirling flows.

This paper presents a computational study of triple flames in swirling flows. We performed and analyzed three-dimensional numerical simulations which start with a nonreacting, premixed, heptane and air mixture with a specified vortex profile. After the initial vortex flow reached a steady state, the mixture was then ignited and a triple flame formed in the vortex flow. Simulations with different swirl numbers showed different triple-flame shapes and different flow fields (with or without vortex breakdown) at the final steady state. The flame and flow structures of these simulations are presented and discussed and this is followed by a vorticity analysis showing how the vortex structures are affected by triple flames leading to different flame shapes. We then discuss how the insights gained from this work can be related to the blue whirl.

2. Background

2.1. Swirling flows and vortex breakdown

Swirling flows occur natually in phenomena, such as tornadoes, dust devils, and fire whirls. They are also of practical importance in swirl combustion systems [6,7] and plasma dynamic systems

* Corresponding author.
E-mail address: xiaoz@terpmail.umd.edu (X. Zhang).

https://doi.org/10.1016/j.combustflame.2022.112364

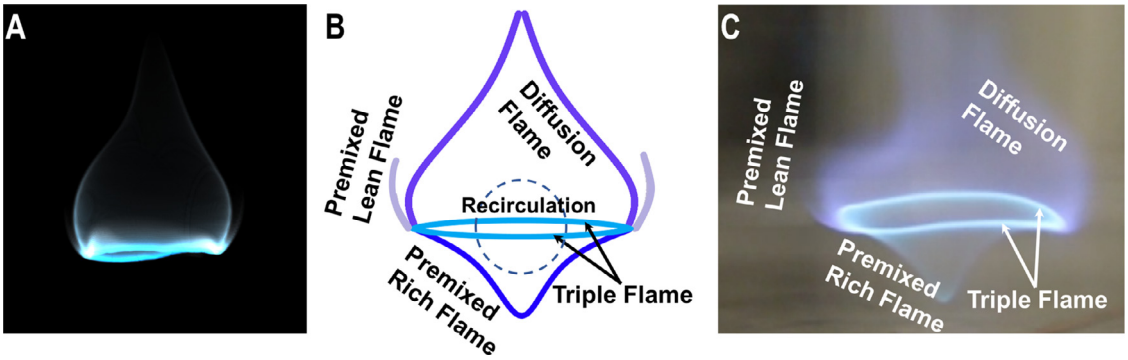

Fig. 1. The flame structure of the blue whirl (taken from [4]). (a) Volume rendering of the heat release rate from the numerical simulation described in [4]. (b) Schematic diagram that summarizes a final result of the blue whirl simulation. (c) Observed blue whirl.

[8]. Without disturbances, swirling flow would normally have an axisymmetric vortex core. The stability of the swirling flow is affected by the ratio of the azimuthal to axial velocity intensities (measured as the swirl level). When the swirl increases to a critical level, a stagnation point with a finite recirculation zone downstream forms around the vortex axis. Vortex breakdown refers to this abrupt change in the vortex structure of the swirling flow.

There are many types of vortex breakdown and they are categorized based on their distinct flow structures. The three major types are the bubble mode, spiral mode, and the double-helix mode [9,10]. Extensive experimental, numerical, and theoretical studies have been performed on its onset, flow structures, formation mechanisms, and controlling parameters. Reviews of vortex breakdown can be found in [11,12].

Vortex breakdown can be both detrimental and beneficial, depending on the application. In aeronautics, vortex breakdown in vortices over highly swept wings of an aircraft can reduce lift and cause dangerous vibrations [13]. For combustion applications, the bubble mode of vortex breakdown can be used to stabilize the flame and enhance fuel and air mixing. The following section includes a more detailed background on applications of swirling flows and vortex breakdown in combustion systems.

2.2. Combustion in swirling flows

Swirling flows are used in many combustion applications, examples of which include gas turbine combustors and jet engines [14]. The key effect of swirl is to produce recirculation zones that improve flame stability and enhance fuel and air mixing, thereby reducing pollution and increasing combustion efficiency[6]. Swirling flames can be sensitive to the operating conditions, which include confinement of the burner [15–18], mode of fuel entry (gaseous or droplet spray [19,20], premixed or non-premixed) and swirl levels [21–24]. Many reviews are available on the dynamics of swirling flames [6,14,25] and swirl burners [26].

Although swirling flames have been studied extensively, they are different from the blue whirl in many aspects. A schematic of typical flow and flame configurations in a swirl burner is shown in Fig. 2. Figure 2a shows the flow field with several low-velocity regions, which are vortex breakdown (VB), centerbody wake (CW), and two shear layers (SL) originating from the inner and outer annulus edges. Flames are stabilized in these low-velocity regions and different flame shapes can form, illustrated in Fig. 2b–e, depending on whether the flame is stabilized in the region preceding the vortex breakdown or in one or both of the shear layers. Visually, the shape of the traditional swirling flames in Fig. 2 is different from the blue whirl in Fig. 1. The swirling flames usually do not have a closed flame surface, but have 'M' or 'V' shapes instead. The blue whirl has a closed flame surface and has a hat shape on the top and a cup shape on the bottom. The relative location of the bubble mode and the flame surface is also different for the swirling flames and the blue whirl. As shown in Fig. 2, the swirling flame is usually stabilized at the upstream-end of the bubble mode or in the low velocity shear layers upstream of the bubble. The blue whirl has flame surfaces both upstream and downstream of the bubble, and in fact, the bubble is enclosed by the flame. Another difference is that swirling flames are usually turbulent whereas the blue whirl is laminar. Moreover, a fundamental difference is that swirling flames are usually fuel-lean whereas the blue whirl has fuel-lean, fuel-rich and diffusion flames which meet as a triple flame.

2.3. Triple flame

A triple flame (also known as a tribrachial flame) forms when the flame propagates through a nonuniform mixture with a mixture fraction gradient perpendicular to the direction of propagation. As shown in Fig. 3, a lean premixed flame forms on the fuel-lean side, a rich premixed flame forms on the fuel-rich side, and the excess fuel and air pass through the flame and diffuse into each other which then form a diffusion flame. The triple flame structure was first reported by Phillips [28] studying flame propagation in mixing layers in coal mines. Later research on triple flames in two-dimensional (2D) mixing layers focused on the effects of mixture fraction gradients, strain rate, and heat release on the flame shape and propagation speed [29–32]. In turbulent combustion, there are local variations in the equivalence ratio of the mixture. Therefore, triple flames are allowed to form and play an important role in autoignition and turbulent flame propagation [33,34]. Triple flames are also important in the stabilization of lifted diffusion flames. The role of triple flames in the stabilization mechanism is reviewed in [35].

Triple flames in various flow configurations are summarized in [35]. Triple flames in swirling flows, however, are not as commonly reported and studied in prior research. One example of a triple flame in a swirling flow was observed in direct numerical simulations by Domingo and Vervisch [36], who focused on flame propagation in turbulent rotating flows. In this study, a triple flame structure was observed, but the shape is different from the blue whirl. The flow configuration in [36] is also different from the blue whirl. In [36], the flow is turbulent, whereas the flow in the blue whirl is laminar. Another example is in a liquid film combustor designed by Pham et al. [37]. The configuration and flow structure, however, are different from the blue whirl. The triple flame in [37] forms near the confining tubular chamber whereas the blue whirl is much smaller than its confining geometry(approximately 5 to 10 times smaller in diameter [1]). Moreover, there is no vortex breakdown in the triple flame in [37] which leads to a different

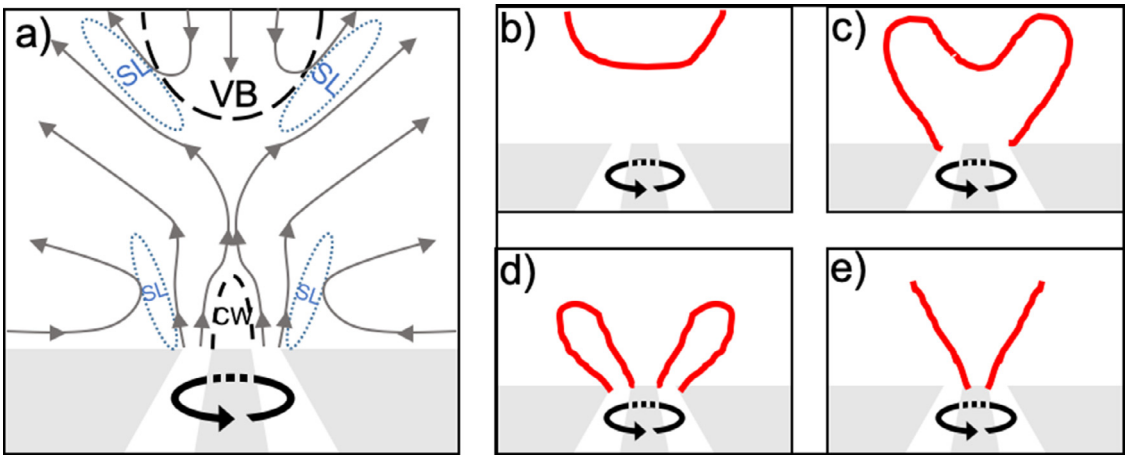

Fig. 2. Schematics of flow field and flame shapes in a swirl burner (adapted from [27]). (a) Flow field. Swirl direction is indicated by the black arrow inside the annular swirling nozzle. Streamlines are shown by grey solid lines with arrows. Black dashed lines indicate vortex breakdown (VB) and centerbody wake (CW). Blue dashed lines indicate shear layers (SL). (b – e) Several possible flame configurations depending on whether the flame is stabilized in the region preceding the VB or in one or both of the SL. Red solid lines indicate flame surface.

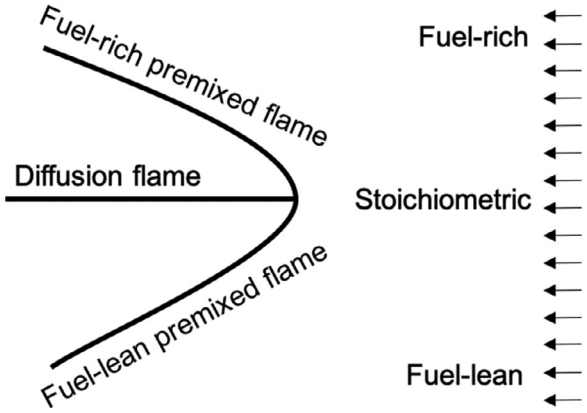

Fig. 3. Schematic diagram of a triple flame.

flame shape compared to the blue whirl. Therefore, a fundamental study of triple flames in swirling flows, especially with vortex breakdown, is needed to help find ways to control the blue whirl and also add to the current knowledge of triple flames in different configurations.

3. Governing Equations

The numerical model solves the time-dependent, three-dimensional, compressible, reactive, Navier-Stokes (NS) equations:

$$\frac{\partial \rho}{\partial t} = -\nabla \cdot (\rho \mathbf{V}) \tag{1}$$

$$\frac{\partial (\rho \mathbf{V})}{\partial t} = -\nabla \cdot (\rho \mathbf{V}\mathbf{V}) - \nabla P - \nabla \cdot \hat{\tau} + \rho \mathbf{g} \tag{2}$$

$$\frac{\partial E}{\partial t} = -\nabla \cdot ((E+P)\mathbf{V}) - \nabla \cdot \left(\mathbf{V} \cdot \hat{\tau}\right) - \nabla \cdot (K \nabla T) + \rho (\mathbf{V} \cdot \mathbf{g}) + \dot{q} \tag{3}$$

$$\frac{\partial \rho Y_i}{\partial t} = -\nabla \cdot (\rho Y_i \mathbf{V}) + \nabla \cdot (\rho D \nabla Y_i) + \rho \dot{\omega}_i \tag{4}$$

$$\hat{\tau} = \rho \nu \left(\frac{2}{3} (\nabla \cdot \mathbf{V}) \mathbf{I} - (\nabla \mathbf{V}) - (\nabla \mathbf{V})^{\dagger} \right) \tag{5}$$

where ρ is density, $\mathbf{V}$ is velocity, E is total energy, P is pressure, Y_i is the mass fraction of species i, $\dot{w}_i$ is the species conversion rate, $\mathbf{g}$ is the gravity vector, $\dot{q}$ is the heat release rate, K is the coefficient of thermal conduction, D is the mass diffusivity, and $\hat{\tau}$ is the viscous stress tensor. The coefficient ν is the kinematic viscosity, $\mathbf{I}$ is a unit matrix, and superscript † indicates the matrix transpose. The total energy is given by

$$E = \rho e + \frac{1}{2} \rho \mathbf{V}, \tag{6}$$

where the specific internal energy e is computed as

$$e = \frac{P}{\rho(\gamma - 1)}. \tag{7}$$

The equation of state is given by

$$P = \rho \frac{R_u}{M_w} T, \tag{8}$$

where R_u is the universal gas constant and M_w is the molecular weight. We assume that kinematic viscosity, diffusion, and heat conduction have the following temperature dependence,

$$\nu = \nu_0 \frac{T^n}{\rho} \qquad \frac{K}{\rho C_p} = \kappa_0 \frac{T^n}{\rho} \tag{9}$$

where ν_0 and κ_0 are constants, $C_p = \gamma R_u / M_w (\gamma - 1)$ is the specific heat at constant pressure, and $n = 0.7$ emulates a typical temperature dependence of these coefficients in reactive hydrocarbon systems.

4. Numerical Methods

In order to calculate this low-speed reactive flow efficiently, a low-Mach-number algorithm, BIC-FCT (the barely implicit correction to flux-corrected transport), is used to solve the hyperbolic fluxes. The detailed procedure is described in [38,39]. The underlying fluid solver is based on fourth-order flux-correxted transport (FCT) [40,41]. In one time step, the solution is first predicted by explicit FCT and then modified by a pressure correction to filter out high frequencies of the sound-wave spectrum. This procedure removes the computational restriction imposed by sound waves, thereby reducing the numerical expense of explicitly integrating the NS equations for low-Mach-number flows. A number of benchmark tests for both nonreactive and reactive flows can be found in [38,39,42].

The effects of diffusion and chemical reactions with heat release for heptane and air mixtures are incorporated into the solver using the CDM (chemical diffusive model) [42–44]. The CDM is different from detailed chemial models, which include multiple species and reaction pathways, in that the CDM reduces the computational cost of complex, 3D computations by minimizing the number of species and reactions that are required to compute bulk combustion properties. Examples of these properties include the flame speed, thickness, and temperature. The CDM used here considers three species (fuel, air, and product) and regulates the conversion from fuel and air to product using a mathematical expression, for example, a polynomial or Arrhenius exponential. In this work, we use an Arrhenius function,

$$\dot{\omega} = A\rho Y \exp(-E_a/R_u T) \quad \dot{q} = q\dot{\omega} \tag{10}$$

to regulate $\dot{q}$ in Eq. 3 and $\dot{\omega}_i$ in Eq. 4. The parameters in this Arrhenius function are the pre-exponential factor A, progress variable Y, and activation energy E_a. The heat release is q. The coefficients A, E_a, and q are calibrated so that the flame properties (flame temperature, speed, and thickness) of heptane-air mixtures are reproduced within a Navier-Stokes computation. The detailed calibration procedure can be found in [39,42,43], and the coefficients for heptane can be found in [39]. The CDM has been used to simulate combustion flows ranging from high-speed denotations [44], to low-speed premixed flames, diffusion flames, and triple flames [4,39,42,45–47].

The diffusion fluxes are solved using second-order central differencing for the spatial derivatives and second order runge-kutta for time integration. Details of how the diffusion terms are incorporated in the integration procedure are described in [38]. These numerical methods were also used to simulate the blue whirl and were succesful in capturing its flow and flame structures [4].

5. Computational Setup and Initial Conditions

There are two major steps taken in the simulations presented in this paper. In the first step, we simulate a vortex flow that is nonreacting and has premixed fuel and air injected into the domain within the vortex core. The nonreacting flow is simulated until it develops to a steady state. Then in the second step, we ignite the fuel-air mixture and let a flame develop until the flow reaches a new steady state.

We specify the initial vortex flow using the Grabowski vortex profile [48,49]. In this profile, the azimuthal, radial, and axial velocities are functions of the radial location r,

$$v_\theta(0 \leqslant r \leqslant R) = \frac{Sr}{R}\left(2 - \left(\frac{r}{R}\right)^2\right) \tag{11}$$

$$v_\theta(R \leqslant r) = \frac{SR}{r} \tag{12}$$

$$v_r(r) = 0 \tag{13}$$

$$v_z(0 \leqslant r \leqslant R) = \alpha + (1-\alpha)\left(\frac{r}{R}\right)^2\left(6 - 8\frac{r}{R} + 3\left(\frac{r}{R}\right)^2\right) \tag{14}$$

$$v_z(R \leqslant r) = 1. \tag{15}$$

Here, the Reynolds number is defined as $Re = v_{z,\infty}R/\nu$, in which R is the radius of the vortex core, and the swirl number is $S = v_\theta(R)/v_{z,\infty}$. The parameter $\alpha = v_{z,c}/v_{z,\infty}$ describes the axial velocity profile. When $\alpha > 1.0$, the axial velocity has a jet-like profile. When $\alpha < 1.0$, the axial velocity has a wake-like profile. For all cases in this paper, we use $\alpha = 1.0$, which corresponds to a uniform axial velocity profile.

The initial pressure is specified using the following equations:

$$P(R \leqslant r) = \rho S^2\left(-\frac{R^2}{2r^2}\right) + P_\infty \tag{16}$$

$$P(0 \leqslant r < R) = \rho S^2\left[\frac{1}{6}\left(\frac{r}{R}\right)^6 - \left(\frac{r}{R}\right)^4 + 2\left(\frac{r}{R}\right)^2 - \frac{7}{6}\right] + P(r = R) \tag{17}$$

which was derived based on the radial force balance in a vortex flow with the Grabowski velocity profile.

For this vortex profile, the controlling parameters are Re, S, α, and R. For all cases in this paper, only the swirl number S is varied while all the other parameters are held constant. An example of the initial azimuthal velocity and pressure profiles are shown in Fig. 4.

The simulations are performed on a 0.1 m × 0.1 m × 0.1 m domain as shown in Fig. 5. We define the z-axis as the axial direction and specifiy the lower axial xy plane as an inflow and the upper axial xy plane as a non-reflecting outflow. The gravity g is specified as 9.81 m/s^2 along the z-axis pointing downward. At the inflow boundary, the Grabowski vortex profile is imposed as described above. Premixed heptane-air mixture is injected from the inflow boundary into the domain within a specified inlet radius. Outside of inlet radius, the inflow is specified to be air with a temperature of 300 K and a pressure of 1 atm. The lateral boundaries are set to be non-reflecting and the pressure is controlled using Bernoullies' equation: $P = P_\infty - \rho V^2/2$, where V is the magnitude of the velocity.

For all cases considered, the flow is initialized with a Grabowski profile throughout the whole domain. An example of the initial azimuthal velocity field is shown in Fig. 5. The initial flow in the domain is specified to be air with a temperature of 300 K and a pressure of 1 atm. A Cartesian mesh is employed with four levels of refinement. The region of refinement is fixed during the calculation. The number of cells on each level is indicated in Fig. 5.

There are three major cases presented in this paper, as shown in Table 1 with their corresponding inflow parameters. These major cases are labeled case 1, case 2a, and case 3, which all have the same $Re = 700$, $\alpha = 1.0$, fuel inlet diameter $d_{fuel} = 3.1$ mm, and equivalence ratio $\phi = 2$. They differ in swirl number, which increased from $S = 0.6$, to $S = 0.8$, to $S = 1.1$. The increase in the swirl number results in different flame shapes and flow structures. For case 2a, however, the resulting flow structure is not very pronounced and the flow features are not visually apparent. Therefore the fuel inlet diameter was increased in case 2b which resulted in a more pronounced flow structure with more visually apparent features. Details of cases 1, 2a, 2b and 3 are described in the following section.

6. Results

6.1. Case 1 - triple flame without vortex breakdown

For case 1, the flow before and after ignition is shown in Fig. 6. Figure 6a shows the flow before ignition, but after it has developed into a steady state from the initial Grabowski vortex profile. Streamlines show the swirling motion of the flow and the volume rendering of the equivalence ratio shows the distribution of the heptane-air mixture before ignition. After reaching this steady state, the mixture is ignited by adding heat to a small region at the center of the vortex, shown by the red box in Fig. 6a. Different ignition locations were simulated and we found that the location does not change the final state. After ignition, a flame develops and the flow evolves into a new steady state, shown in Fig. 6b.

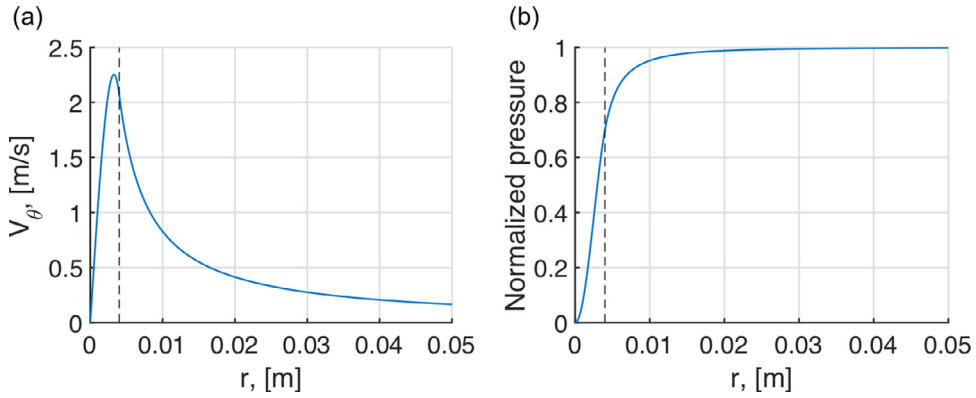

Fig. 4. Grabowski vortex profile with $Re = 700, S = 0.8, \alpha = 1$ and $R = 0.4$ cm: (a) Azimuthal velocity along the radial direction; (b) Pressure along the radial direction. The dashed line indicates the vortex core radius R.

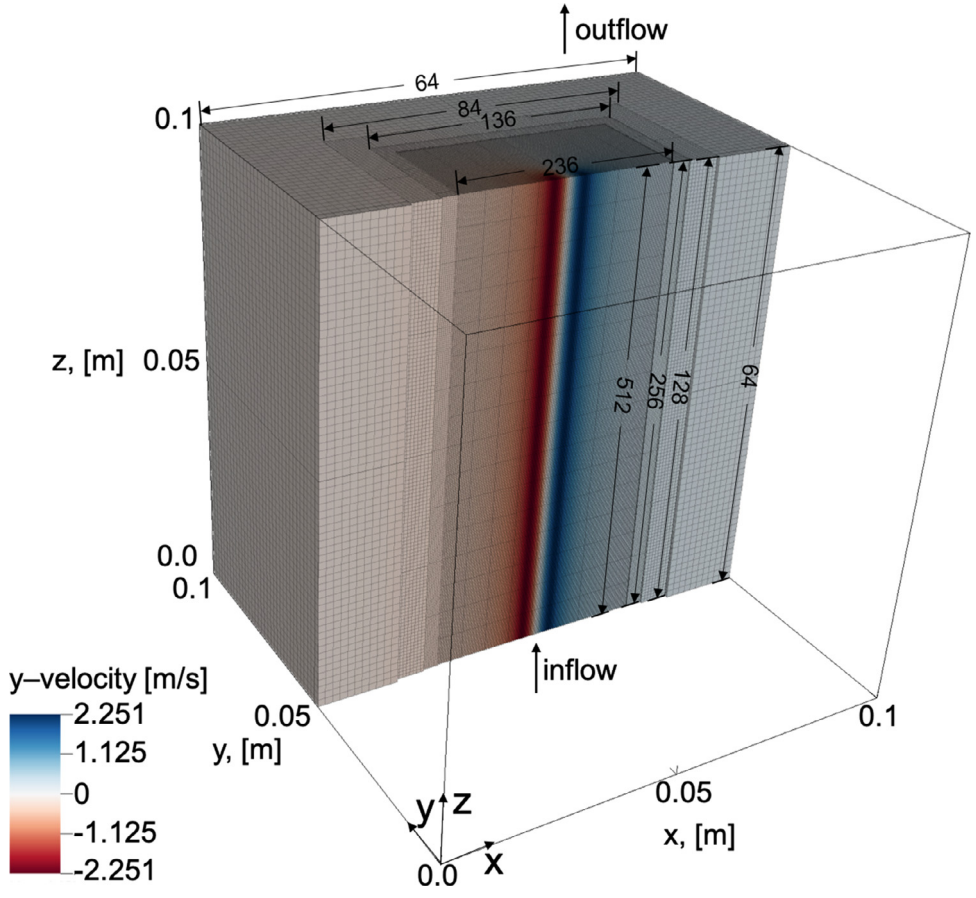

Fig. 5. Computational domain and mesh with superimposed initial velocity field.

Table 1
Conditions, parameters, and general observations

	Conditions and parameters					Observations	
	S	Re	α	d_{fuel}[mm]	ϕ	Before ignition	After ignition
case 1	0.6	700	1.0	3.1	2.0	No VB	No VB, forms triple flame with premixed rich flame curving upwards.
case 2a	0.8	700	1.0	3.1	2.0	No VB	Two VB (one within the flame and one above the flame), forms triple flame with premixed rich flame curving downwards.
case 2b	0.8	700	1.0	4.0	2.0	No VB	Same as 2a, except for a larger region of VB within the flame.
case 3	1.1	700	1.0	3.1	2.0	VB	Two VB (one at the lower part and one at the upper part of the flame), forms triple flame with both premixed rich flame and diffusion flame curving downwards.

* VB refers to vortex breakdown.

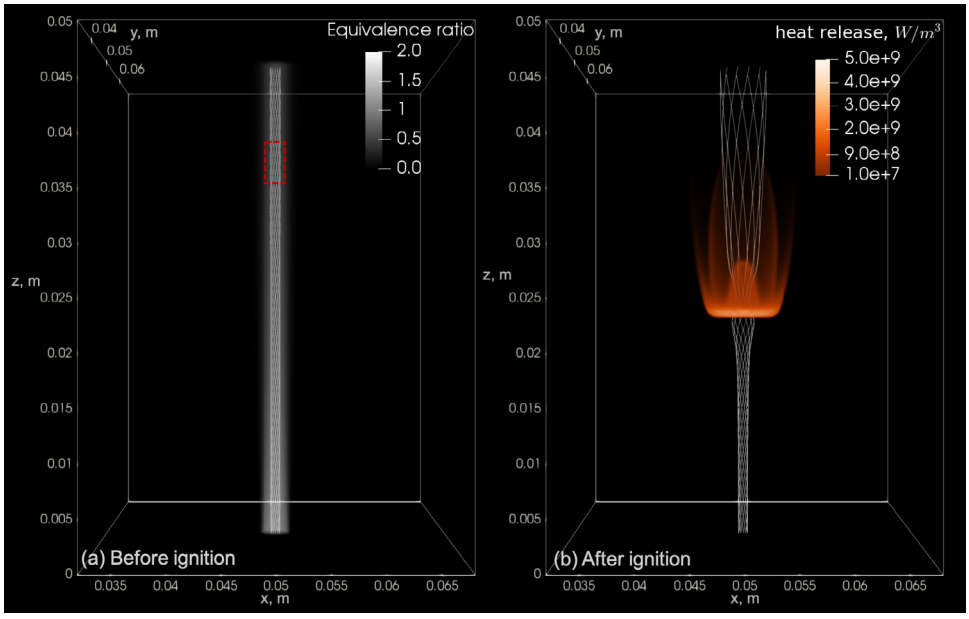

Fig. 6. Case 1: Triple flame in a swirling flow without vortex breakdown. The initial condition of the flow is specified using a Grabowski vortex profile, with $Re = 700$, $S = 0.6$, $\alpha = 1.0$. (a) Before ignition. Streamlines are overlaid on top of a volume rendering of equivalence ratio. The $\phi = 2$ heptane-air mixture is injected from the bottom within a specified diameter $d_{fuel} = 3.1$ mm. The red rectangle indicates the region where the flow will be ignited. (b) After ignition. Streamlines are overlaid on top of a volume rendering of heat-release rate.

The flame is visualized by a volume rendering of heat release rate in Fig. 6b. The flame structure can be delineated by three distinct layers. The first layer is the radially outer-most flame, which has a wing-like flame surface. Moving towards the center axis, there are two flame surfaces that both curve upward, with one extending further in the axial direction than the other. These three layers of flames meet at the bottom and form a bright ring which has the most heat release. The streamlines in Fig. 6b show that the flame causes the flow downstream to diverge and that there is no reversed flow region, indicating that there is no vortex breakdown.

Additional diagnostics of the flame structure are shown in Fig. 7. Figure 7a shows a map of the flame index [50], which indicates whether the flame is a premixed or diffusion flame. The flame index is calculated as

$$I_f = \frac{\nabla Y_{\text{Fuel}} \cdot \nabla Y_{\text{Ox}}}{\nabla Y_{\text{Fuel}} ||\nabla Y_{\text{Ox}}|}, \tag{18}$$

where Y_{Fuel} and Y_{Ox} are mass fractions of fuel and oxidizer. Premixed flames are indicated by heat release rate contours that overlap with regions of $I_f > 0$, marked in Fig. 7a by the circled a and b markers. Similarly, diffusion flames are indicated by heat release rate contours that overlap with regions of $I_f < 0$, marked in Fig. 7a by the circled c marker. The contour of equivalence ratio of unity, shown by the white contour line in Fig. 7a marked by "1", demarcates the region of fuel-rich flow that is inside the contour and fuel-lean flow outside of it. This, combined with the heat release contour and flame index, shows that the flame marked by "a" is a rich premixed flame, the flame marked by "b" is a lean premixed flame, and the flame marked by "c" is a diffusion flame. All three flames meet together and form a triple flame. Figure 7b shows a map of the fuel mass fraction, which indicates that most of the fuel is burned downstream of the flame (92.6% of the fuel is consumed as measured at the outlet). Figure 7c is a temperature map which shows that the peak temperature is around 2200 K in the diffusion flame. The flame structure in this case is similar to the lifted flame shown in Fig. 1d in [35], except that the flame here is in a vortex flow whereas the flame in Fig. 1d in [35] is in a non-swirling jet flow.

The flow conditions of case 1 is shown in Fig. 8. The tangential velocity, shown in Fig. 8a, maintains the Grabowski profile near the inflow, as specified by the inflow boundary condition. As the flow moves towards the flame and downstream of it, the flow maintains a vortex structure but the peak tangential velocity decreases and the vortex core grows wider. Figure 8b shows a map of the radial velocity. In the region near the inflow, there is no radial velocity due to the boundary condition. In the region near the flame, especially in the triple flame and just upstream of it, the flow experiences radial acceleration and divergence due to the blockage caused by the flame. Figure 8 c shows a map of the axial velocity. At the inflow, the axial velocity is uniform as specified by the boundary condition. As the flow moves from the inflow towards the flame, the axial velocity decreases until the flow reaches the triple flame. Then, as the flow passes through the triple flame and moves further downstream, the axial velocity increases. Finally, the flow moves downstream from the diffusion flame and the axial velocity decreases again. Although there are two regions with decelerating axial velocity, the decelerations are not sufficient to cause negative axial velocity, indicating that there is no vortex breakdown in this flowfield.

6.2. Case 2 - triple flame with bubble modes of vortex breakdown

Compared to case 1, case 2a has a higher swirl number of $S = 0.8$ (case 1 has $S = 0.6$). The flow before and after ignition is shown in Fig. 9. Figure 9a shows the non-reacting vortex flow at the steady state developed from the initial Grabowski profile before ignition. Figure 9b shows the flow and flame at a new steady state after ignition. Similar to case 1, there are also three layers of flames. The outer most flame has a wing-like flame surface. Moving towards the center axis, instead of having two flames that curve upward as in case 1, the upper flame surface still curves upwards while the lower flame surface curves downward in this case. This is due to vortex breakdown (shown by the streamlines), which produces downward axial velocities around the lower flame surface. The streamlines in Fig. 9b diverge around the region of vortex breakdown and further diverge downstream of the flame. The

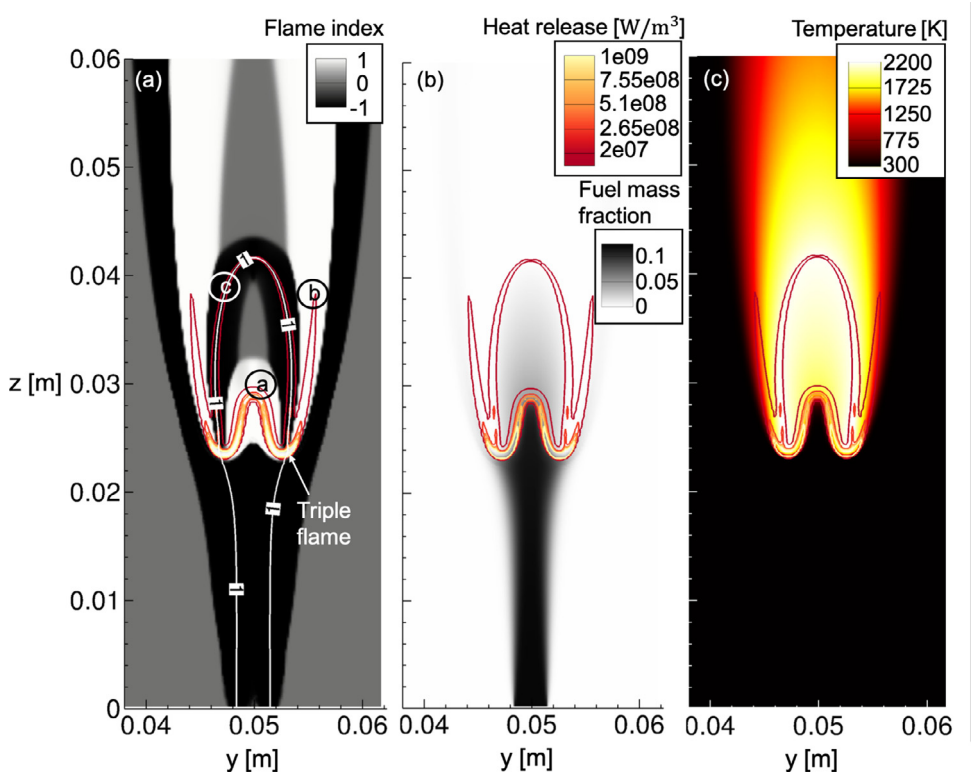

Fig. 7. Case 1: Combustion diagnostics on slices through the center of the computational domain. (a) Flame index. The line with marker "1" is the contour line of an equivalence ratio of unity. The equivalence ratio is larger than 1 inside the contour and smaller than 1 outside of the controur. (b) Fuel mass fraction. (c) Temperature. Contours of heat release rate are superimposed on top to indicate reaction regions. Slices are taken from a zoomed-in region.

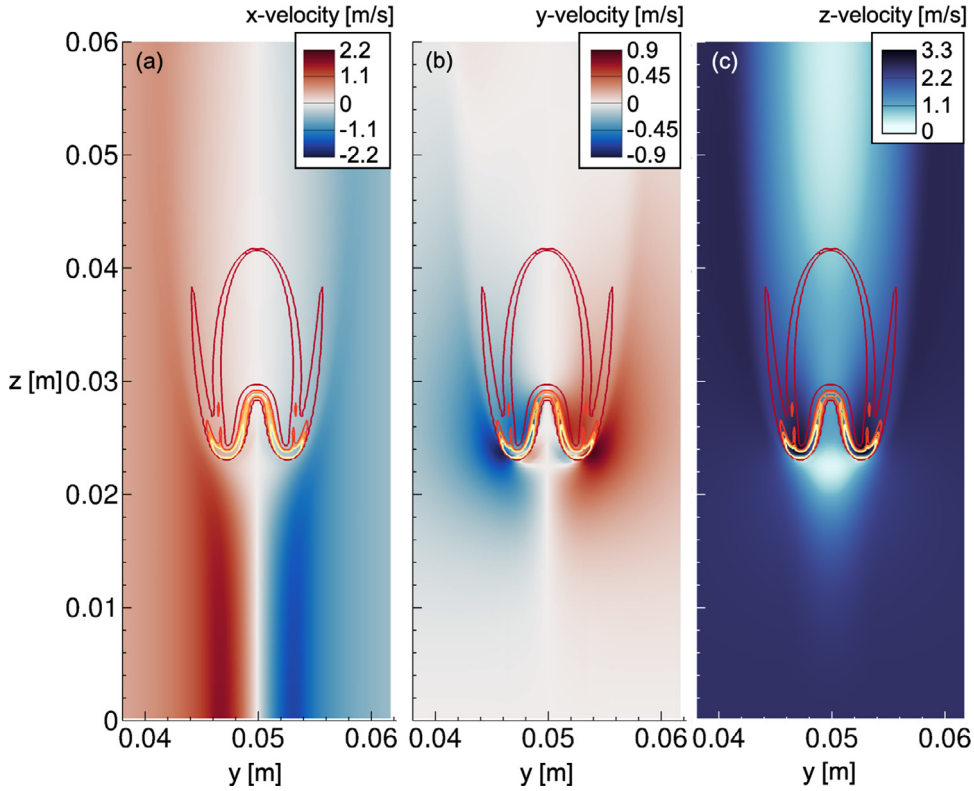

Fig. 8. Case 1: Flow diagnostics on slices through the center of the computational domain. (a) Tangential velocity. (b) Radial velocity. (c) Axial velocity. Contours of heat release rate are superimposed on top to indicate reaction regions. Slices are taken from a zoomed-in region.

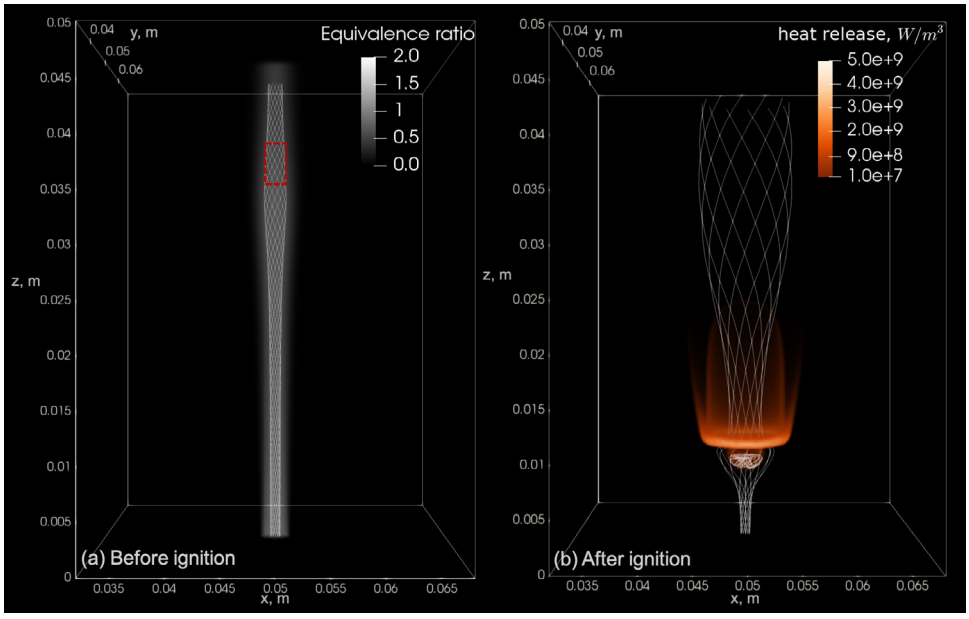

Fig. 9. Case 2a: Triple flame in a swirling flow with bubble modes of vortex breakdown. Compared with case 1, all the parameters are kept the same, except for an increase in the swirl number. The initial condition of the flow is specified using a Grabowski vortex profile, with $Re = 700$, $S = 0.8$, $\alpha = 1.0$. (a) Before ignition. Streamlines are overlaid on top of a volume rendering of equivalence ratio. The $\phi = 2$ heptane-air mixture is injected from the bottom within a specified diameter $d_{fuel} = 3.1$ mm. The red rectangle indicates the region where the flow will be ignited. (b) After ignition. Streamlines are overlaid on top of a volume rendering of heat-release rate.

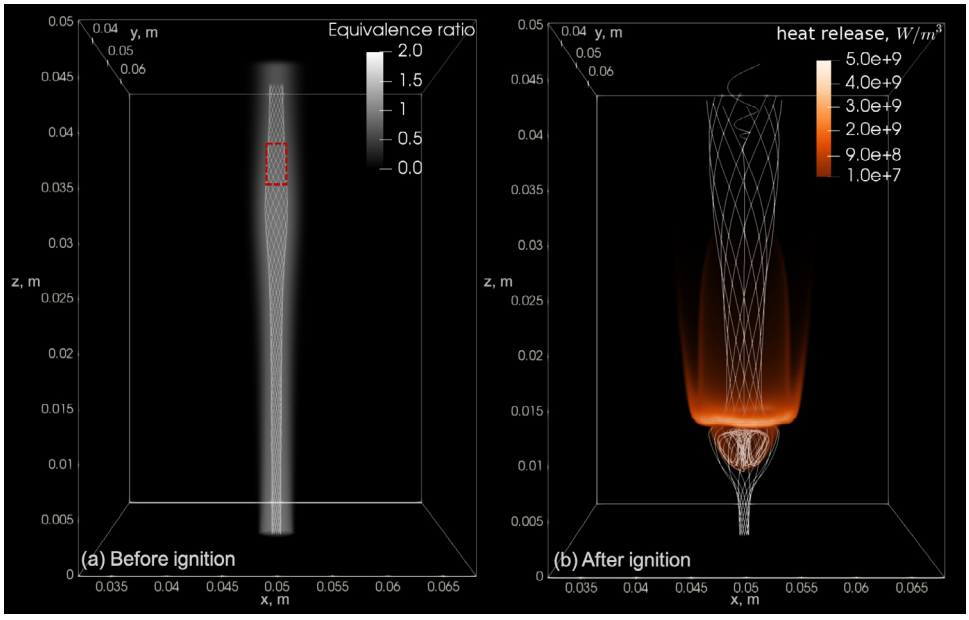

Fig. 10. Case 2b: Triple flame in a swirling flow with bubble modes of vortex breakdown. Compared with case 2a, all the parameters are kept the same, except for an increase in the fuel inlet diameter. This results in a larger bubble mode inside the flame, which is more pronounced than in case 2a. The initial condition of the flow is specified using a Grabowski vortex profile, with $Re = 700$, $S = 0.8$, $\alpha = 1.0$. (a) Before ignition. Streamlines are overlaid on top of a volume rendering of equivalence ratio. The $\phi = 2$ heptane-air mixture is injected from the bottom within a specified diameter $d_{fuel} = 4$ mm. The red rectangle indicates the region where the flow will be ignited. (b) After ignition. Streamlines are overlaid on top of a volume rendering of heat-release rate.

second divergence is due to a secondary vortex breakdown downstream of the flame. Since the size of the vortex breakdown structures is not as visually apparent as the flame, we calculated another case with a wider fuel inlet ($d_{fuel} = 4$ mm), which produced more visually apparent flow and flame structures.

The flow and flame for this case with a wider fuel inlet, case 2b, is shown in Fig. 10. Compared to case 2a, case 2b has a similar flow and flame structure. The major differences are that the size of the flame in case 2b, shown in Fig. 10b, is larger than the flame of case 2a, shown in Fig. 9b, and the lower flame along the center axis is larger and protrudes further downward relative to the ring. The streamlines in Fig. 10b show that the the vortex breakdown inside the flame is also larger the vortex breakdown seen in case 2a in Fig. 9b. The axial location of the secondary vortex breakdown downstream is also shown by a twisted streamline near the center axis. Because case 2b has a more pronounced structure than that of case 2a, the detailed flame and flow diagnostics for case 2 with $S = 0.8$ are performed with case 2b.

A detailed visualization of the flame structure is shown in Fig. 11. Figure 11a shows a map of the flame index, overlaid with a

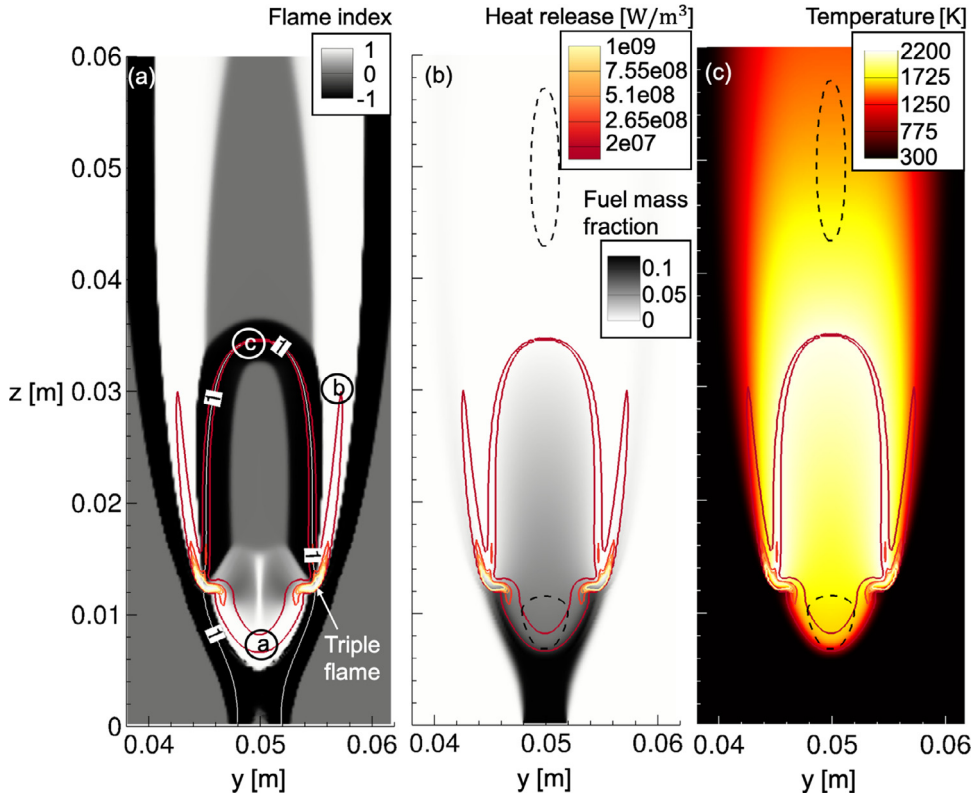

Fig. 11. Case 2b: Combustion diagnostics on slices through the center of the computational domain. (a) Flame index. The line with marker "1" is the contour line of an equivalence ratio of unity. The equivalence ratio is larger than 1 inside the contour and smaller than 1 outside of the controur. (b) Fuel mass fraction. (c) Temperature. Contours of heat release rate are superimposed on top to indicate reaction regions. Dashed lines in (b) and (c) indicate the reversed flow regions. Slices are taken from a zoomed-in region.

contour of heat release and a contour of the stochiometric equivalence ratio ($\phi = 1$). Following the same analysis as done for case 1, the flame in region a is a rich premixed flame, in b is a lean premixed flame, and in c is a diffusion flame. All of these three flames meet together and form a triple flame. Figure 11b shows a map of the fuel mass fraction, which indicates that most of the fuel is burned downstream of the flame (91.9% of the fuel is consumed as measured at the outlet). Figure 11c is a temperature map which shows that the peak temperature is around 2200 K in the diffusion flame, similar to that of case 1. This flame structure and shape is similar to the blue whirl (Fig. 1), and the peak temperature is also similar to the blue whirl in experimental measurements [51] and numerical simulations [4,5].

The detailed flow structure of case 2b in terms of maps of tangential, radial, and axial velocities are shown in Fig. 12. The overall flow field is similar to that in case 1. As the flow propagates downstream of the flame, Fig. 12a shows the tangential velocity decreasing and the vortex core widening. The radial velocity, shown by Fig. 12b, is initially zero near the inflow due to the boundary condition. The flow diverges as it propagates toward the flame due to the blockage effect. The axial velocity, shown by Fig. 12c, enters the domain with a uniform profile as specified by the boundary condition. Similar to case 1, the axial velocity decreases as the flow approaches the flame. What is different here, however, is that the axial velocity experiences stronger deceleration than in case 1, leading to reverse flow and a bubble mode of vortex breakdown. This reverse flow region pushes the rich premixed flame downward in case 2b, whereas the rich premixed flame curves upward in case 1. Downstream of the diffusion flame, there is a secondary reversed flow region, which indicates a secondary bubble mode of vortex breakdown. This secondary vortex breakdown, however, does not affect the flame. The flow structure in case 2b, especially for the bubble mode within the flame (Fig. 1), is similar to the blue whirl [4,5]. The difference between this case and the blue whirl is that in the blue whirl, there has been no observed secondary vortex breakdown downstream [4,5].

6.3. Case3 - triple flame with larger bubble modes of vortex breakdown

Compared with previous cases, the swirl number in case 3 is further increased to $S = 1.1$. The flow before and after ignition is shown in Fig. 13. Figure 13a shows the nonreacting vortex flow at the steady state developed from the specified Grabowski profile before ignition. This larger swirl number results in a bubble mode of vortex breakdown in the non-reacting initial flow, which is different from earlier cases.

The mixture is then ignited around the region of vortex breakdown, shown by the dashed line in Fig. 13a. Figure 13b shows the flow and flame at a new steady state after ignition. As in cases 1 and 2, there are three layers of flames, with the outer most flame having a wing-like flame surface and two flames along the center axis. Unlike cases 1 and 2, both of these two flames now curve downward. This is due to the two vortex breakdown regions, shown by the streamlines in Fig. 13b. The lower flame surface curves downward due to the upstream vortex breakdown. The upper flame surface curves downward due to the downstream, larger vortex breakdown. Compared with case 2 in which there are also two vortex breakdown regions, the downstream vortex breakdown in case 3 is further upstream and impinges on the flame, therefore affecting the flame shape.

The flame structure of case 3 is shown in Fig. 14. Figure 14a shows a map of the flame index. Combine with the contour of the equivalence ratio of unity, the flame in region a is a rich premixed

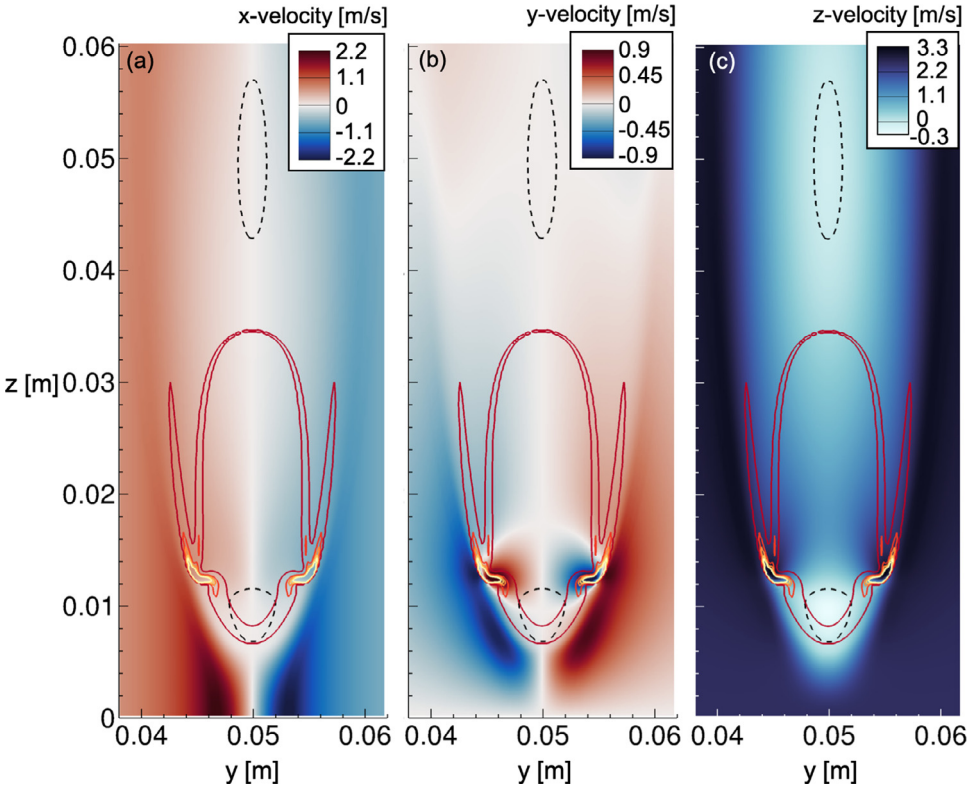

Fig. 12. Case 2b: Flow diagnostics on slices through the center of the computational domain. (a) Tangential velocity. (b) Radial velocity. (c) Axial velocity. Contours of heat release rate are superimposed on top to indicate reaction regions. Dashed lines indicate the reversed flow regions. Slices are taken from a zoomed-in region.

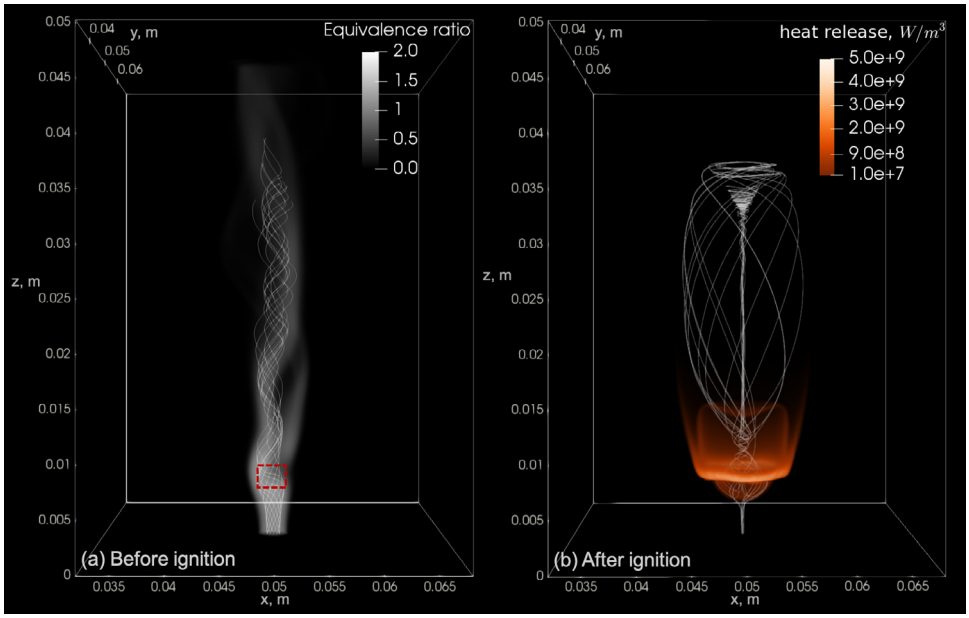

Fig. 13. Case 3: Triple flame in a swirling flow with larger bubble modes of vortex breakdown. Compared with case1 and 2a, all the parameters are kept the same, except for a further increase in the swirl number. The initial condition of the flow is specified using a Grabowski vortex profile, with $Re = 700$, $S = 1.1$, $\alpha = 1.0$. (a) Before ignition. Streamlines are overlaid on top of a volume rendering of equivalence ratio. The $\phi = 2$ heptane-air mixture is injected from the bottom within a specified diameter $d_{fuel} = 3.1$ mm. The red rectangle indicates the region where the flow will be ignited. (b) After ignition. Streamlines are overlaid on top of a volume rendering of heat-release rate.

flame, in b is a lean premixed flame, and in c is a diffusion flame. All of these three flames meet and form a triple flame. This is similar to the previous cases. Figure 14b shows a map of the fuel mass fraction, which indicates that most of the fuel is burned downstream of the flame. Figure 14c is a temperature map which shows that, similar to the previous cases, the peak temperature is around 2200 K in the diffusion flame. Unlike the previous cases, the region with high temperature does not extend as far downstream due to the second vortex breakdown. The temperture around the second vortex breakdown is about 1000 K.

The flow structure of case 3 in terms of maps of tangential, radial, and axial velocities are shown in Fig. 15. The overall flow

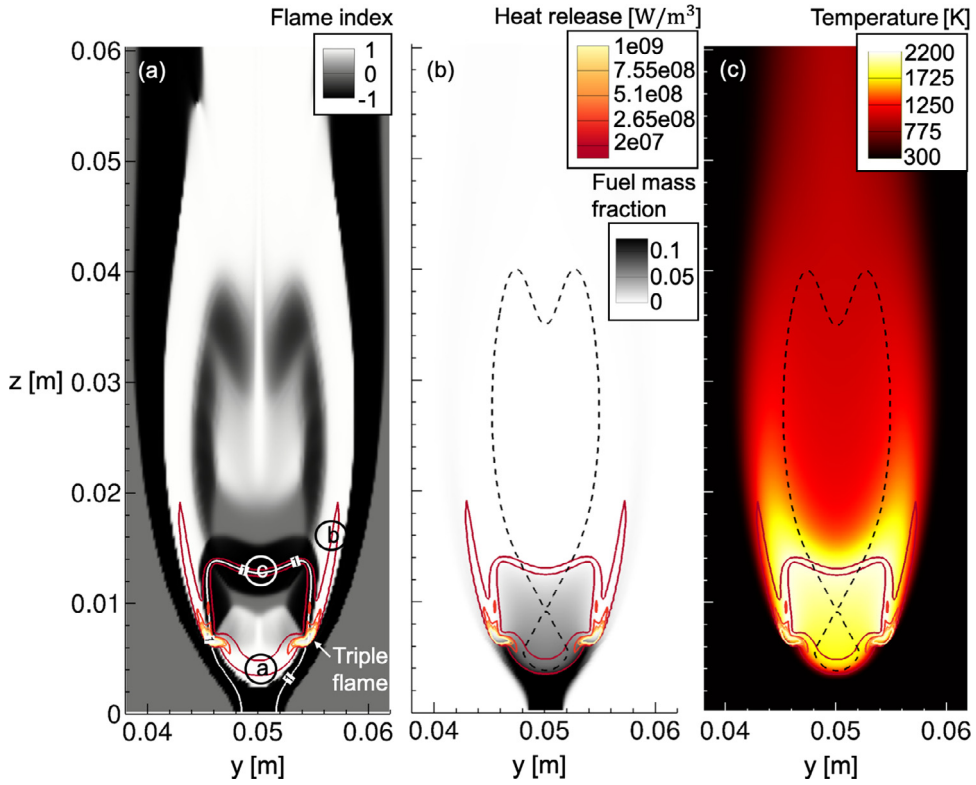

Fig. 14. Case 3: Combustion diagnostics on slices through the center of the computational domain. (a) Flame index. The line with marker "1" is the contour line of an equivalence ratio of unity. The equivalence ratio is larger than 1 inside the contour and smaller than 1 outside of the controur. (b) Fuel mass fraction. (c) Temperature. Contours of heat release rate are superimposed on top to indicate reaction regions. Dashed lines in (b) and (c) indicate the reversed flow regions. Slices are taken from a zoomed-in region.

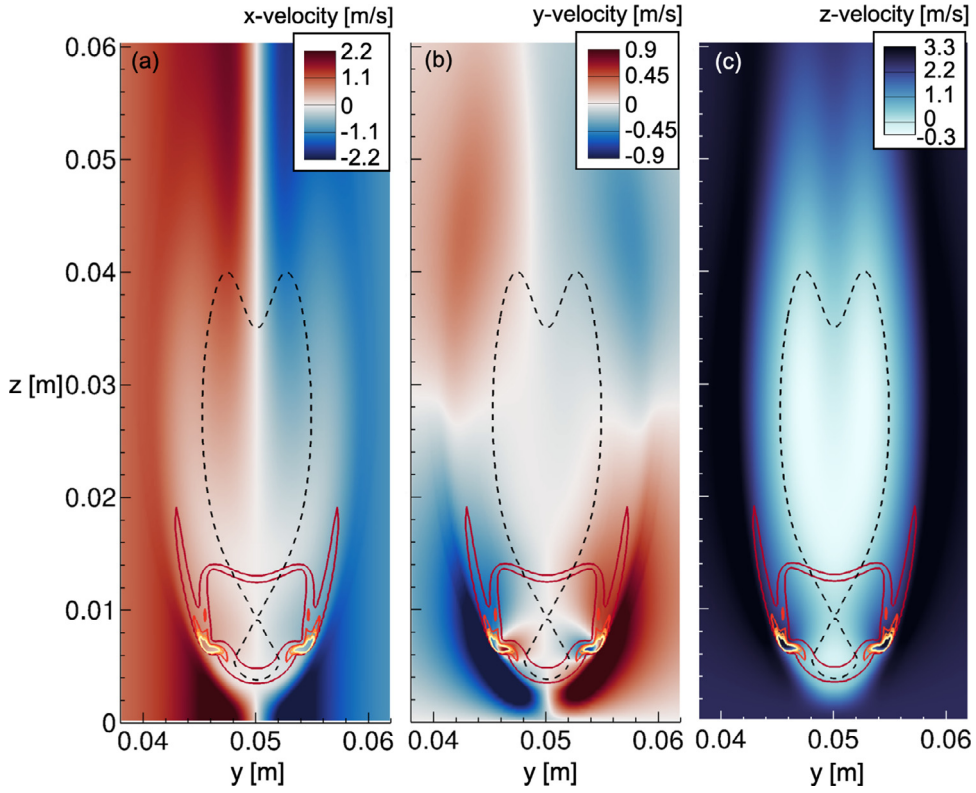

Fig. 15. Case 3: Flow diagnostics on slices through the center of the computational domain. (a) Tangential velocity. (b) Radial velocity. (c) Axial velocity. Contours of heat release rate are superimposed on top to indicate reaction regions. Dashed lines indicate the reversed flow regions. Slices are taken from a zoomed-in region.

field is similar to the previous cases. The tangential velocity near the bottom inlet boundary follows the specified Grabowski profile. As the flow propagates downstream of the flame, around the two vortex breakdown regions, the tangential velocity shows a vortex structure with a lower peak velocity and a wider vortex core. Further downstream of the second vortex breakdown, however, the vortex structure recovers with an increase in the peak tangential velocity and decrease in the vortex core size. The radial velocity at the bottom inlet boundary is essentially zero, as specified by the Grabowski profile. As the flow approaches the flame, radial velocity increases due to the divergence caused by the blockage effect. The axial velocity is uniform near the inlet boundary. The axial velocity decelerates as the flow approaches the flame and forms the first reversed flow region (bubble mode of vortex breakdown). This region of reversed flow curves the rich premixed flame downward. A larger reversed flow region forms downstream of the diffusion flame, indicating that there is a secondary bubble mode of vortex breakdown. This secondary vortex breakdown is different from that in case 2 because it impinges on the diffusion flame and therefore curves it downward.

7. Vorticity Analysis

As shown above, after ignition, each case develops a triple flame. The shape of each flame, however, varies from case to case due to the differences in flow structures after ignition. These differences appear in the occurance and location of the bubble mode of vortex breakdown with respect to the burning. To better understand the origin of the different flame shapes, we investigate the characterstics of the bubble mode after ignition in each case.

The bubble mode of vortex breakdown refers to a recirculation zone along the vortex axis [52]. Vorticity that generates negative axial velocity (opposes the axial flow) contributes to the occurrence and growth of the bubble mode, whereas vorticity that generates positive axial velocity acts to the mitigation of the bubble mode [53–55]. Thus, in order to understand why the different cases have different bubble mode characterstics, we analyze how vorticity is affected by ignition in each case.

We analyze the vorticity ω using the inviscid transport equation, Eq. 19, in a similar manner to the analysis performed in [53]. As shown on the right side of Eq. 19, the changes of vorticity are caused by three mechanisms. The first term on the right represents stretching and tilting, the second term represents the volume expansion or contraction due to heat addition or extraction, and the third term represents baroclinic torque.

$$\frac{\partial}{\partial t}(\boldsymbol{\omega}) + (\mathbf{U}\cdot\nabla)\boldsymbol{\omega} = (\boldsymbol{\omega}\cdot\nabla)\mathbf{U} - \boldsymbol{\omega}(\nabla\cdot\mathbf{U}) + \frac{1}{\rho^2}(\nabla\rho\times\nabla p) \quad (19)$$

If we calculate the differences in each of these terms before and after ignition, we can then isolate which contributes the most to the generation of vorticity that produces either positive or negative axial velocity, therefore the mitigation or enhancement of the bubble mode. Figures 16,17, 18 show these results. As the bubble mode is quasi-axisymmetric, we take a center y-z plane to analyze changes in vorticity. On this plane, the properties of x-vorticity are presented since it is the only vorticity that contributes to changes in axial velocity (in the z-direction). The x-vorticity has a rotational axis that is perpendicular to the plane and is positive pointing out of the plane and negative pointing into the plane.

Figure 16 shows the changes of x-vorticity for case 1 before and after the flame develops. Figure 16a shows the changes in x-vorticity due to stretching and tilting. Figure 16b shows the changes in x-vorticity due to volume expansion. Figure 16c shows the changes in x-vorticity due to baroclinic torque. The rotation direction of vorticity is indicated by the arrows. The vorticities in Figs. 16a and c generate negative axial velocity (downwards) near the center axis, which promote vortex breakdown. Whereas the vorticities in Fig. 16b generate positive axial velocity (upwards) near the center axis, which mitigate vortex breakdown. Between these two competing effects, the dominant one dictates whether vortex beakdown develops or not. Thus, by considering the result that there is no vortex breakdown in case 1, we see that the vorticities in Fig. 16b caused by volume expansion dominate. Therefore, the vorticity changes due to volume expansion dominate in case 1 and cause the flame surface of the rich premixed flame to curve upwards.

A similar analysis was performed for case 2b, and the changes of x-vorticity before and after the flame develops are shown in Fig. 17. The vorticities in Figs. 17a and c generate negative axial velocity (downwards) near the center axis, which promote vortex breakdown. Whereas the vorticity in Fig. 17b generates positive axial velocity (upwards) near the center axis, which mitigates vortex breakdown. By considering the result that there is a bubble mode of vortex breakdown within the lower part of the flame (indicated by dashed lines in Fig. 17), the vortex stretching and tilting (Fig. 17a) and the baroclinic torque (Fig. 17c) overpower the volume expansion (Fig. 17b) and result in the formation of vortex breakdown. Moreover, comparing the effects in Fig. 17a and Fig. 17c, we see that the magnitude of vorticity change in Fig. 17a is larger than that in Fig. 17c. Therefore, for case 2b, the vortex stretching and tilting in Fig. 17a dominates and contributes to the formation of bubble mode of vortex breakdown, which in turn causes the flame surface of the rich premixed flame to curve downwards.

Figure 18 shows the changes of x-vorticity for case 3 before and after the flame develops. The vorticities in Figs. 18a and c generate negative axial velocity (downwards) near the center axis, thus promoting vortex breakdown. In contrast, the vorticity in Fig. 18b generates positive axial velocity (upwards) near the center axis, thus mitigating vortex breakdown. At the steady state after ignition, we see that there are two bubble modes near the flame region (indicated by dashed lines in Fig. 18). For the bubble mode at the lower part of the flame, there are two competing effects contributing to vorticity, as shown in Figs. 18a,c and Fig. 18b. The vorticities in Figs. 18a,c overpower the vorticities in Fig. 18b, and this results in the formation of the lower vortex breakdown. Moreover, the magnitude of vorticity changes in Fig. 18a is larger than that in Fig. 18c. Therefore, the effect in Fig. 18a, vortex stretching and tilting, is the dominant effect that contributes to the formation of the lower vortex breakdown, which causes the flame surface of the rich premixed flame to curve downwards. For the bubble mode at the upper part of the flame, vortex stretching and tilting, shown in Fig. 18a, is the only effect on vorticity. Therefore, vortex stretching and tilting is the dominant effect that contributes to the formation of the upper vortex breakdown, causing the flame surface of the diffusion flame to curve downwards.

8. Discussion

The vorticity analysis shows that there are two competing effects on vorticity generation due to ignition. One of these effects generates the vorticity that produces negative axial velocity near the center axis. This effect promotes the formation of bubble mode of vortex breakdown. The other effect generates vorticity that produces positive axial velocity near the center axis. This effect mitigates the formation of bubble mode. Whether vortex breakdown develops or not at the steady state after ignition depends on which effect dominates.

For the three cases presented in this study, volume expansion dominates and mitigates the formation of the bubble mode in the case with the smallest swirl number (case 1). For the cases with larger swirl numbers (case 2b and case 3), vortex stretching

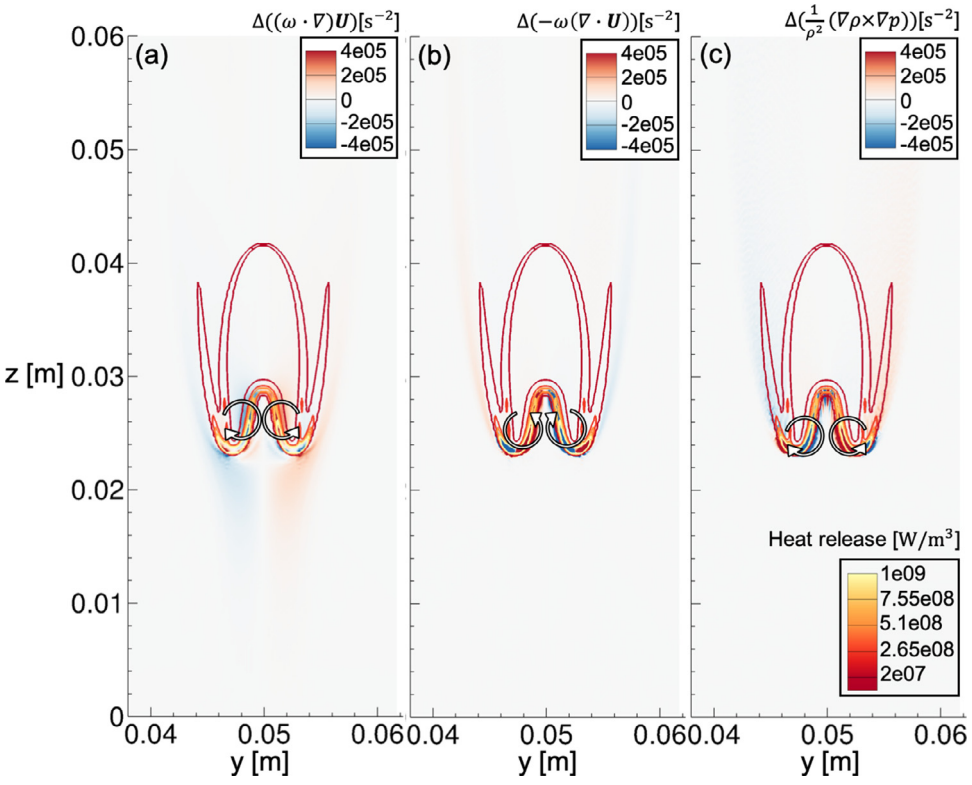

Fig. 16. Case 1: Influence of ignition to x-vorticity on a center y-z plane. (a) Changes in x-vorticity due to vortex stretching and tilting. (b) Changes in x-vorticity due to volume expansion. (c) Changes in x-vorticity due to baroclinic torque. Contours of heat release rate are superimposed on top to indicate reaction regions.

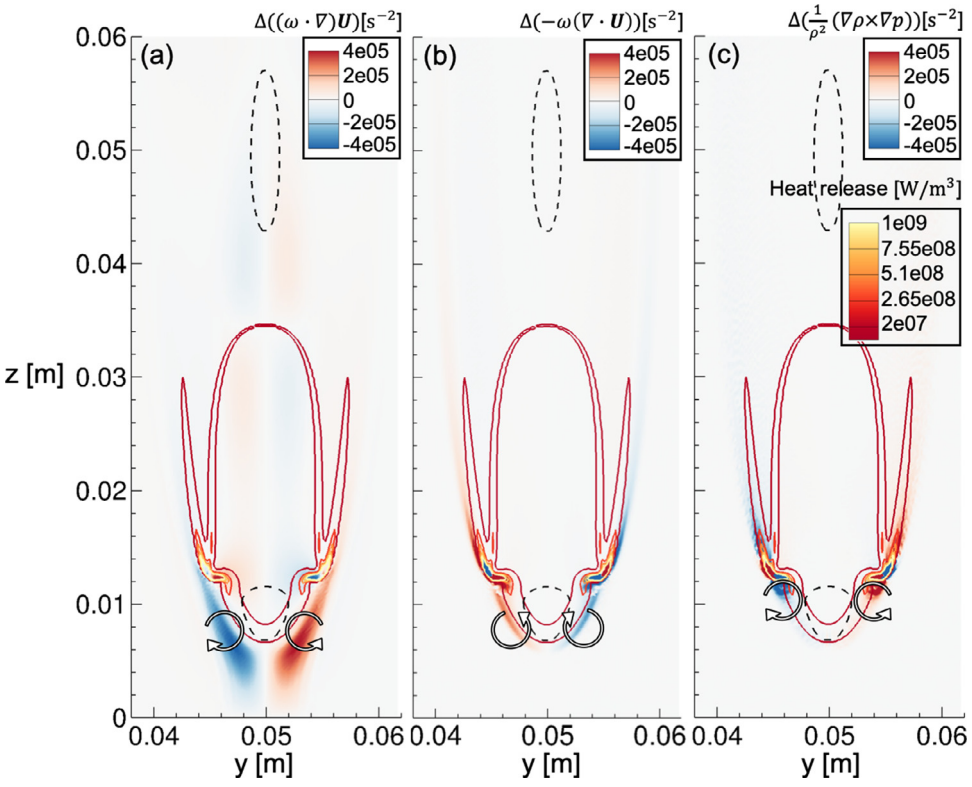

Fig. 17. Case 2b: Influence of ignition to x-vorticity on a center y-z plane. (a) Changes in x-vorticity due to vortex stretching and tilting. (b) Changes in x-vorticity due to volume expansion. (c) Changes in x-vorticity due to baroclinic torque. Contours of heat release rate are superimposed on top to indicate reaction regions. Dashed lines indicate the reversed flow regions.

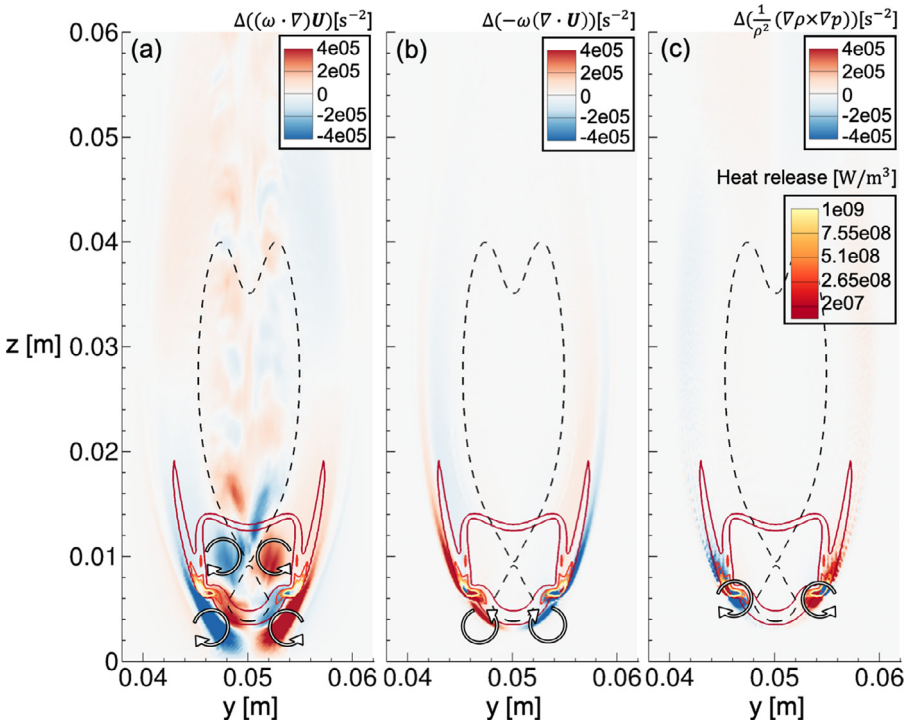

Fig. 18. Case 3: Influence of ignition to x-vorticity on a center y-z plane. (a) Changes in x-vorticity due to vortex stretching and tilting. (b) Changes in x-vorticity due to volume expansion. (c) Changes in x-vorticity due to baroclinic torque. Contours of heat release rate are superimposed on top to indicate reaction regions. Dashed lines indicate the reversed flow regions.

and tilting dominates and promotes the formation of the bubble mode. In case 2b, this effect and baroclinic torque generate a vortex breakdown within the lower part of the flame and a small, secondary vortex breakdown above the flame. For the case with the largest swirl number (case 3), the effect of both vortex stretching and tilting and baroclinic torque are stronger and not only generate a vortex breakdown within the lower part of the flame, but also generate a large, secondary vortex breakdown that impinges on the upper part of the flame. This trend is consistent with the trend of vortex breakdown in nonreacting flows, that is, a larger swirl number is more conducive to form vortex breakdown and the bubble mode is more pronounced [48].

This study was motivated by the blue whirl, but the result is not limited to understanding the blue whirl. Instead, it is more general in that it contributes to understanding triple flames in swirling flows. The blue whirl was discovered unintentionally in a laboratory [1] and its flame and flow properties remained a mystery until recent studies revealed a specific combination of flow properties – a triple flame in a swirling flow with vortex breakdown. The three triple flames in swirling flows in this study, one with flow and flame structures similar to the blue whirl and two other cases that have different flame shapes, broaden understanding and lead us to believe that the blue whirl might be only one configuration among many different configurations of triple flames in swirling flows. In this study, we focused on the effect of swirl number on triple flames in swirling flows. Other parameters controlling vortex breakdown, such as Reynolds number and the jet-like or wake-like axial velocity profile, and combustion parameters, such as fuel inlet diameter and whether the mixture is premixed or non-premixed, should be investigated in future studies to further explain this unique combustion phenomenon.

This study has also given us insight into the blue whirl. One remaining question about the blue whirl is whether we can create it in a more controlled way so its beneficial burning properties can be put to use. We have seen that the blue whirl evolves spontaneously from a fire whirl and self-regulates the inflow conditions during the transition process [1]. Creating the blue whirl in this way, however, is difficult because it is difficult to produce the exact conditions on demand. The flame at steady state in case 2b has similar flow and flame structures to the blue whirl. This indicates that it is possible to create a blue-whirl-like flame in a more controlled way by igniting a controlled nonreacting flow. This study gives one set of parameters that produces a blue-whirl structure. Future studies of different parameters should provide a wider range of potentially useful conditions.

Another intriguing question about the blue whirl is that whether it can be increased in size. The major difficulty in answering this question is that the formation conditions in which the blue whirl forms in terms of the controlling parameters are not fully known. It is difficult and expensive in both experiments and simulations to explore an unknown, large-scale parameter space. By starting from the set of parameters in this study as a first step, a more complete parametric study of triple flames in swirling flows could provide a more complete map of parameters controlling the blue whirl.

Another question about the blue whirl is whether we can bypass the large, dangerous fire-whirl stage and create the blue whirl directly. This study shows that we can create a flame with similar flow and flame structures to the blue whirl using premixed fuel-air mixtures with controlled flow at the base, passing the fire-whirl stage. For all the cases in this study, the flames develop without going through a fire-whirl stage. An example of the flame development is shown in Fig. 19. There is a difference, however, between this study and the blue whirl in [1,4]. The fuel and air are premixed in this study whereas in [1,4], the fuel and air are initially separated. The configuration and computational setup in this study could, however, be used as a starting point to address the question of whether we can create a blue whirl in [1,4] with nonpremixed fuel without going through a fire whirl by replacing the premixed inflow with a nonpremixed fuel.

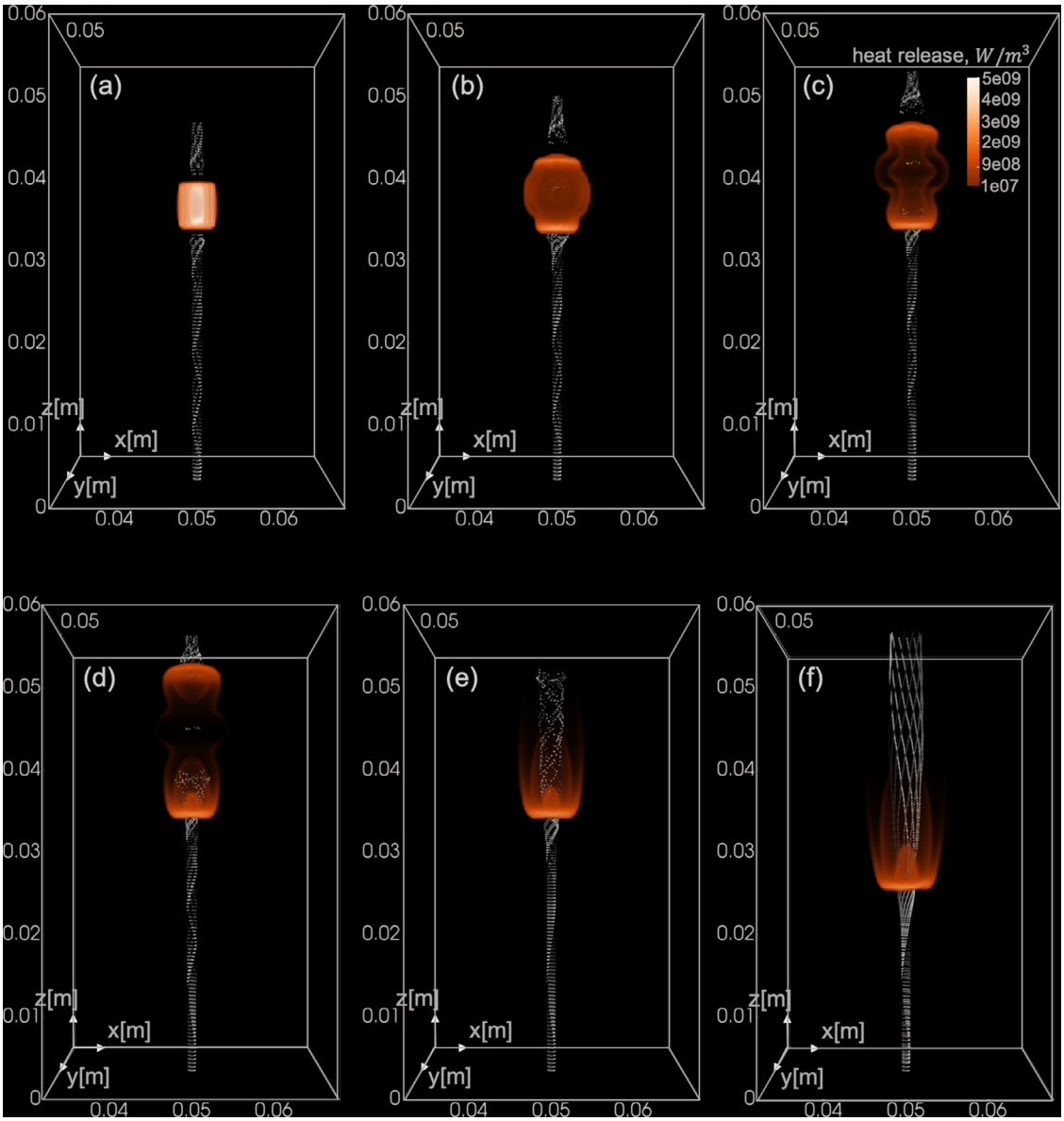

Fig. 19. Flame development for case 1 from (a) ignition to (f) steady state. Streaklines indicated by white, grey, and black particles are superimposed to show the flow structure.

9. Summary

This paper has presented a numerical study of triple flames in swirling flows. For this study, we solved the 3D, unsteady, compressible, reactive, NS equations. The simulations began with a specified vortex profile and with a premixed, heptane-air mixture injected at the center of vortex. After the initial vortex flow developed into a steady state, the mixture was ignited and a triple flame formed in the vortex flow.

There were three cases presented in this paper, each with a different swirl number. For the case with the smallest swirl number ($S = 0.6$), there was no vortex breakdown at the steady state before ignition. After ignition, a triple flame formed and the flow decelerated due to blockage from the flame. In this case, however, there was no vortex breakdown. The surfaces of the diffusion flame and the rich premixed flame both curved upwards due to the positive (upwards) axial velocity.

For the case with a larger swirl number ($S = 0.8$), there was also no vortex breakdown at the steady state before ignition. After ignition, a triple flame formed and two bubble modes of vortex breakdown developed, one above the flame and one within the lower part of the flame. The surface of the diffusion flame was not affected by these two bubbles and curved upwards, similar to that in the previous case. The surface of the rich premixed flame, however, curved downwards due to the reversed (downwards) axial flow in the lower bubble. The structure of the flow and flame in this case was similar to that of the blue whirl.

The case with the largest swirl number ($S = 1.1$) developed a bubble mode of vortex breakdown at the steady state before ignition. After ignition, a triple flame formed and two bubble modes of vortex breakdown developed, one which impinged on the upper part of the flame and one which was within the lower part of the flame. The reversed axial flow in the upper bubble caused the surface of the diffusion flame to curve downwards. The reversed axial flow in the lower bubble caused the surface of the rich premixed flame to curve downwards.

Changes in vorticity before and after ignition in each case were analyzed to investigate why the occurrence and location of the

bubble mode is different in each case, thereby causing different flame shapes. There are three mechanisms that affect vorticity. They are vortex stretching and tilting, volume expansion, and baroclinic torque. For the case with the smallest swirl number ($S = 0.6$), volume expansion dominated among the three effects. The volume expansion effect generated vorticity that produced positive axial velocity near the axis and mitigated vortex breakdown. For the cases with larger swirl numbers ($S = 0.8$ and $S = 1, 1$), vortex stretching and tilting dominated and generated vorticity that produced negative axial velocity near the vortex axis, thereby promoting vortex breakdown.

This study focused on understanding the effect of swirl number on triple flames in swirling flows. Future studies should investigate other parameters, such as Reynolds number, fuel inlet diameter and whether the mixture is premixed or non-premixed.

This study also provided insight into the blue whirl. The results shown here suggest that the blue whirl might be one configuration among many different configurations of triple flames in swirling flows. Furthermore, the results also suggest that the blue whirl could be created in a more controlled way by igniting a controlled nonreacting vortex flow. The numerical configuration in this study could be used for a more complete parametric study on the blue whirl. Such a study could help answer whether we can increase the size of the blue whirl. This study also shows that we can produce a blue-whirl-like flame using a premixed fuel-air mixture and bypass the fire-whirl stage.

Declaration of Competing Interest

The authors declare that they have no known competing financial interests or personal relationships that could have appeared to influence the work reported in this paper.

Acknowledgments

This work was supported by the National Science Foundation Grant CBET 2050771 and the O'Donnell Foundation Chair at Texas A&M University. Computations were performed on the Deepthought2 cluster at the University of Maryland and the Extreme Science and Engineering Discovery Environment (XSEDE) [56] Stampede2 at the Texas Advanced Computing Center through allocations TG-CTS180016 and TG-CTS190040. Computations in this work used 200,000 CPU hours using Intel Xeon Skylake nodes and 50,000 CPU hours using Dell PowerEdge C8220 nodes with dual Intel Ivy Bridge E5-2680v2 processor.

References

[1] H. Xiao, M.J. Gollner, E.S. Oran, From fire whirls to blue whirls and combustion with reduced pollution, Proceedings of the National Academy of Sciences 113 (34) (2016) 9457–9462.
[2] S.B. Hariharan, P.M. Anderson, H. Xiao, M.J. Gollner, E.S. Oran, The blue whirl: Boundary layer effects, temperature and OH* measurements, Combustion and Flame 203 (2019) 352–361.
[3] P. Anderson, L. Price, S. Gunukula, D.T. Tran, Blue whirl phenomenon: A potential fuel-flexible and soot-free combustion technology, Energy & Fuels 34 (9) (2020) 11708–11711.
[4] J.D. Chung, X. Zhang, C.R. Kaplan, E.S. Oran, The structure of the blue whirl revealed, Science Advances 6 (33) (2020) eaba0827.
[5] J. Carpio, W. Coenen, A. Sánchez, E. Oran, F. Williams, Numerical description of axisymmetric blue whirls over liquid-fuel pools, Proceedings of the Combustion Institute 38 (2) (2021) 2041–2048.
[6] N. Syred, J. Beer, Combustion in swirling flows: a review, Combustion and Flame 23 (2) (1974) 143–201.
[7] A.K. Gupta, D.G. Lilley, N. Syred, Swirl flows, Tunbridge Wells (1984).
[8] A. Klimov, V. Bityurin, B. Tolkunov, K. Zhirnov, M. Plotnikova, K. Minko, V. Kutlaliev, Longitudinal vortex plasmoid created by capacity HF discharge, 46th AIAA Aerospace Sciences Meeting and Exhibit, 2008. Paper 2008-1386
[9] T. Sarpkaya, On stationary and travelling vortex breakdowns, Journal of Fluid Mechanics 45 (3) (1971) 545–559.
[10] T. Sarpkaya, Vortex breakdown in swirling conical flows, AIAA Journal 9 (9) (1971) 1792–1799.
[11] O. Lucca-Negro, T. O'doherty, Vortex breakdown: a review, Progress in Energy and Combustion Science 27 (4) (2001) 431–481.
[12] M. Hall, Vortex breakdown, Annual Review of Fluid Mechanics 4 (1) (1972) 195–218.
[13] A.M. Mitchell, J. Délery, Research into vortex breakdown control, Progress in Aerospace Sciences 37 (4) (2001) 385–418.
[14] S. Candel, D. Durox, T. Schuller, J.F. Bourgouin, J.P. Moeck, Dynamics of swirling flames, Annual Review of Fluid Mechanics 46 (2014) 147–173.
[15] A.J. De Rosa, S.J. Peluso, B.D. Quay, D.A. Santavicca, The effect of confinement on the structure and dynamic response of lean-premixed, swirl-stabilized flames, Journal of Engineering Gas Turbines and Power 138 (6) (2016).
[16] K.J. Nogenmyr, H.J. Cao, C.K. Chan, R.K. Cheng, Effects of confinement on premixed turbulent swirling flame using large eddy simulation, Combustion Theory and Modelling 17 (6) (2013) 1003–1019.
[17] N. Syred, K. Dahman, Effect of high levels of confinement upon the aerodynamics of swirl burners, Journal of Energy 2 (1) (1978) 8–15.
[18] A.E. Khalil, J.M. Brooks, A.K. Gupta, Impact of confinement on flowfield of swirl flow burners, Fuel 184 (2016) 1–9.
[19] R. Hadef, B. Lenze, Measurements of droplets characteristics in a swirl-stabilized spray flame, Experimental Thermal and Fluid Science 30 (2) (2005) 117–130.
[20] D.E. Cavaliere, J. Kariuki, E. Mastorakos, A comparison of the blow-off behaviour of swirl-stabilized premixed, non-premixed and spray flames, Flow, Turbulence and Combustion 91 (2) (2013) 347–372.
[21] Y. Huang, V. Yang, Effect of swirl on combustion dynamics in a lean-premixed swirl-stabilized combustor, Proceedings of the Combustion Institute 30 (2) (2005) 1775–1782.
[22] V. Tangirala, R. Chen, J.F. Driscoll, Effect of heat release and swirl on the recirculation within swirl-stabilized flames, Combustion Science and Technology 51 (1-3) (1987) 75–95.
[23] A. Umemura, K. Tomita, Rapid flame propagation in a vortex tube in perspective of vortex breakdown phenomena, Combustion and Flame 125 (1-2) (2001) 820–838.
[24] W.T. Ashurst, Flame propagation along a vortex: the baroclinic push, Combustion Science and Technology 112 (1) (1996) 175–185.
[25] D.G. Lilley, Swirl flows in combustion: a review, AIAA Journal 15 (8) (1977) 1063–1078.
[26] Y.M. Al-Abdeli, A.R. Masri, Review of laboratory swirl burners and experiments for model validation, Experimental Thermal and Fluid Science 69 (2015) 178–196.
[27] M. Malanoski, M. Aguilar, D.H. Shin, T. Lieuwen, Flame leading edge and flow dynamics in a swirling, lifted flame, Combustion Science and Technology 186 (12) (2014) 1816–1843.
[28] H. Phillips, Flame in a buoyant methane layer, Symposium (Int.) Combustion 10 (1) (1965) 1277–1283.
[29] J. Dold, Flame propagation in a nonuniform mixture: analysis of a slowly varying triple flame, Combustion and Flame 76 (1) (1989) 71–88.
[30] L.J. Hartley, J.W. Dold, Flame propagation in a nonuniform mixture: analysis of a propagating triple-flame, Combustion Science and Technology 80 (1-3) (1991) 23–46.
[31] P.N. Kioni, B. Rogg, K. Bray, A. Linán, Flame spread in laminar mixing layers: the triple flame, Combustion and Flame 95 (3) (1993) 276–290.
[32] G. Ruetsch, L. Vervisch, A. Linán, Effects of heat release on triple flames, Physics of Fluids 7 (6) (1995) 1447–1454.
[33] P. Domingo, L. Vervisch, Triple flames and partially premixed combustion in autoignition of non-premixed turbulent mixtures, Symposium (Int.) Combustion 26 (1) (1996) 233–240.
[34] T. Poinsot, Using direct numerical simulations to understand premixed turbulent combustion, Symposium (Int.) Combustion 26 (1) (1996) 219–232.
[35] S.H. Chung, Stabilization, propagation and instability of tribrachial triple flames, Proceedings of the Combustion Institute 31 (1) (2007) 877–892.
[36] P. Domingo, L. Vervisch, DNS of partially premixed flame propagating in a turbulent rotating flow, Proceedings of the Combustion Institute 31 (1) (2007) 1657–1664.
[37] T.K. Pham, D. Dunn-Rankin, W.A. Sirignano, Flame structure in small-scale liquid film combustors, Proceedings of the Combustion Institute 31 (2) (2007) 3269–3275.
[38] X. Zhang, J.D. Chung, C.R. Kaplan, E.S. Oran, The barely implicit correction algorithm for low-mach-number flows, Computers & Fluids 175 (2018) 230–245.
[39] J.D. Chung, X. Zhang, C.R. Kaplan, E.S. Oran, The barely implicit correction algorithm for low-mach-number flows II: Application to reactive flows, Computers & Fluids 210 (2020) 104650.
[40] J.P. Boris, D.L. Book, Flux-corrected transport. i. SHASTA, a fluid transport algorithm that works, Journal of Computational Physics 11 (1) (1973) 38–69.
[41] J.P. Boris, A.M. Landsberg, E.S. Oran, J.H. Gardner, LCPFCT-A flux-corrected transport algorithm for solving generalized continuity equations, Technical Report, NAVAL RESEARCH LAB WASHINGTON DC, 1993.
[42] J.D. Chung, X. Zhang, C.R. Kaplan, E.S. Oran, Low-Mach-number simulation of diffusion flames with the chemical-diffusive model, AIAA Scitech 2019 Forum, 2019. Paper 6.2019-2169
[43] C.R. Kaplan, A. Özgen, E.S. Oran, Chemical-diffusive models for flame acceleration and transition-to-detonation: genetic algorithm and optimisation procedure, Combustion Theory and Modelling 23 (1) (2019) 67–86.
[44] D. Kessler, V. Gamezo, E. Oran, Simulations of flame acceleration and deflagra-

tion-to-detonation transitions in methane–air systems, Combustion and Flame 157 (11) (2010) 2063–2077.
[45] X. Zhang, J.D. Chung, C.R. Kaplan, E.S. Oran, Simulations of a triple flame and fire whirl using the bic low-mach-number algorithm, Proceedings of the 27th International Colloquium on the Dynamics of Explosions and Reactive Systems (2019). Paper 228
[46] J.D. Chung, X. Zhang, C.R. Kaplan, E.S. Oran, Three-dimensional navier-stokes simulations of non-premixed reactive vortex breakdown, Proceedings of the 27th International Colloquium on the Dynamics of Explosions and Reactive Systems (2019). Paper 227
[47] J.D. Chung, X. Zhang, E.S. Oran, C. Kaplan, Numerical simulations of a fire whirl burning gaseous heptane, AIAA Scitech 2020 Forum, 2020. Paper 6.2020-0431
[48] M. Ruith, P. Chen, E. Meiburg, T. Maxworthy, Three-dimensional vortex breakdown in swirling jets and wakes: direct numerical simulation, Journal of Fluid Mechanics 486 (2003) 331–378.
[49] W.J. Grabowski, S. Berger, Solutions of the Navier-Stokes equations for vortex breakdown, Journal of Fluid Mechanics 75 (3) (1976) 525–544.
[50] H. Yamashita, M. Shimada, T. Takeno, A numerical study on flame stability at the transition point of jet diffusion flames, Symposium (Int.) Combustion 26 (1) (1996) 27–34.
[51] S.B. Hariharan, E.T. Sluder, M.J. Gollner, E.S. Oran, Thermal structure of the blue whirl, Proceedings of the Combustion Institute 37 (3) (2019) 4285–4293.
[52] S. Leibovich, The structure of vortex breakdown, Annual Review of Fluid Mechanics 10 (1) (1978) 221–246.
[53] F. Kiesewetter, M. Konle, T. Sattelmayer, Analysis of combustion induced vortex breakdown driven flame flashback in a premix burner with cylindrical mixing zone, Journal of Engineering Gas Turbines and Power 129 (4) (2007) 929–936.
[54] J. Lopez, Axisymmetric vortex breakdown part 1. confined swirling flow, Journal of Fluid Mechanics 221 (1990) 533–552.
[55] G. Brown, J. Lopez, Axisymmetric vortex breakdown part 2. physical mechanisms, Journal of Fluid Mechanics 221 (1990) 553–576.
[56] J. Towns, T. Cockerill, M. Dahan, I. Foster, K. Gaither, A. Grimshaw, V. Hazlewood, S. Lathrop, D. Lifka, G.D. Peterson, R. Roskies, J.R. Scott, N. Wilkins-Diehr, XSEDE: Accelerating scientific discovery, Computing in Science & Engineering 16 (5) (2014) 62–74.